LA-UR-15-24614 (Accepted Manuscript)

Effect of soil property uncertainties on permafrost thaw projections: A calibration-constrained analysis

Harp, Dylan Robert
Atchley, Adam Lee
Painter, Scott L
Coon, Ethan
Wilson, Cathy Jean
Romanovsky, Vladimir E
Rowland, Joel C.

Provided by the author(s) and the Los Alamos National Laboratory (0000-00-00).

To be published in: Cryosphere Discussion, Vol. 9, 3351–3404, 2015

DOI to publisher's version: 10.5194/tcd-9-3351-2015

Permalink to record: http://permalink.lanl.gov/object/view?what=info:lanl-repo/lareport/LA-UR-15-24614

Disclaimer:
Approved for public release. Los Alamos National Laboratory, an affirmative action/equal opportunity employer, is operated by the Los Alamos National Security, LLC for the National Nuclear Security Administration of the U.S. Department of Energy under contract DE-AC52-06NA25396. Los Alamos National Laboratory strongly supports academic freedom and a researcher's right to publish; as an institution, however, the Laboratory does not endorse the viewpoint of a publication or guarantee its technical correctness.

The Cryosphere Discuss., 9, 3351–3404, 2015
www.the-cryosphere-discuss.net/9/3351/2015/
doi:10.5194/tcd-9-3351-2015
© Author(s) 2015. CC Attribution 3.0 License.

The Cryosphere Discussions
Open Access

This discussion paper is/has been under review for the journal The Cryosphere (TC).
Please refer to the corresponding final paper in TC if available.

Effect of soil property uncertainties on permafrost thaw projections: a calibration-constrained analysis

D. R. Harp[1], A. L. Atchley[1], S. L. Painter[2], E. T. Coon[1], C. J. Wilson[1], V. E. Romanovsky[3], and J. C. Rowland[1]

[1]Earth and Environmental Sciences Division, Los Alamos National Laboratory, Los Alamos, NM, USA
[2]Climate Change Science Institute, Environmental Sciences Division, Oak Ridge National Laboratory, Oak Ridge, TN, USA
[3]Geophysical Institute, University of Alaska, Fairbanks, USA

Received: 05 May 2015 – Accepted: 29 May 2015 – Published: 29 June 2015

Correspondence to: D. R. Harp (dharp@lanl.gov)

Published by Copernicus Publications on behalf of the European Geosciences Union.

Abstract

The effect of soil property uncertainties on permafrost thaw projections are studied using a three-phase subsurface thermal hydrology model and calibration-constrained uncertainty analysis. The Null-Space Monte Carlo method is used to identify soil hydrothermal parameter combinations that are consistent with borehole temperature measurements at the study site, the Barrow Environmental Observatory. Each parameter combination is then used in a forward projection of permafrost conditions for the 21st century (from calendar year 2006 to 2100) using atmospheric forcings from the Community Earth System Model (CESM) in the Representative Concentration Pathway (RCP) 8.5 greenhouse gas concentration trajectory. A 100-year projection allows for the evaluation of intra-annual uncertainty due to soil properties and the inter-annual variability due to year to year differences in CESM climate forcings. After calibrating to borehole temperature data at this well-characterized site, soil property uncertainties are still significant and result in significant intra-annual uncertainties in projected active layer thickness and annual thaw depth-duration even with a specified future climate. Intra-annual uncertainties in projected soil moisture content and Stefan number are small. A volume and time integrated Stefan number decreases significantly in the future climate, indicating that latent heat of phase change becomes more important than heat conduction in future climates. Out of 10 soil parameters, ALT, annual thaw depth-duration, and Stefan number are highly dependent on mineral soil porosity, while annual mean liquid saturation of the active layer is highly dependent on the mineral soil residual saturation and moderately dependent on peat residual saturation. By comparing the ensemble statistics to the spread of projected permafrost metrics using different climate models, we show that the effect of calibration-constrained uncertainty in soil properties, although significant, is less than that produced by structural climate model uncertainty for this location.

1 Introduction

Increasing Arctic air and permafrost temperatures (Serreze et al., 2000; Jones and Moberg, 2003; Hinzman et al., 2002; Romanovsky et al., 2007), the resulting increase in the thickness of soil that thaws on an annual basis (Romanovsky and Osterkamp, 1995), and the potential for greenhouse gas release due to the ensuing decomposition of previously frozen organic carbon (Koven et al., 2011; Schaefer et al., 2011) provide motivation for developing robust numerical projections of the thermal hydrological trajectory of Arctic tundra in a warming climate. Projections of permafrost thaw and the associated potential for greenhouse gas release from the accelerated decomposition of previously frozen carbon are subject to several sources of uncertainty, including (but not limited to) structural uncertainties in the climate models; uncertainty about the model forcings/inputs in the future (scenario uncertainty in the typology of Walker et al., 2003); parametric uncertainties in soil and surface properties that control the downward propagation of thaw fronts; and structural uncertainties in the surface and subsurface thermal hydrological models.

Previous efforts to characterize uncertainty in permafrost thaw projections have mostly focused on climate model structural uncertainties and climate scenario uncertainties, presumably because of an implicit assumption that those two sources of uncertainty overwhelm the other sources. However, recent large-scale model comparisons suggest that a substantial portion of projected permafrost uncertainties is a result of structural model differences in land surface/subsurface schemes (Slater and Lawrence, 2013; Koven et al., 2013), particularly how subsurface thermal hydrologic processes are represented (Koven et al., 2013) rather than simply climate variation. Although those studies focused on structural uncertainty in surface and subsurface models and not on soil property uncertainty, the reported sensitivity to the subsurface model suggests that uncertainty in soil properties may also contribute significantly to overall uncertainty in thaw projections.

The bulk hydrothermal properties of soil that control the active layer thickness (ALT, i.e. the depth of soil that thaws on an annual basis) (Neumann, 1860; Stefan, 1891; Romanovsky and Osterkamp, 1997; Peters-Lidard et al., 1998; Kurylyk et al., 2014) vary among sites and locally within a single site, in particular being sensitive to the local organic matter content and bulk porosity (Letts et al., 2000; Price et al., 2008; O'Donnell et al., 2009; Hinzman et al., 1991; Chadburn et al., 2015). Langer et al. (2013) identify the soil composition uncertainties, particularly the soil ice/water content, to have the largest effect on ALT. Intermediate to large-scale thermal simulations of ALT are known to be sensitive to soil properties (Hinzman et al., 1998; Rawlins et al., 2013). Because of this sensitivity, large-scale Earth System Models (ESMs) were recently updated to include layers of moss and peat in order to better represent subsurface thermal conditions (Beringer et al., 2001; Lawrence and Slater, 2008; Subin et al., 2012). Despite the recognition of soil property uncertainty and heterogeneity as important contributors to uncertainties in permafrost conditions and extent, global and regional studies that address permafrost future conditions and extent typically apply broad soil texture classifications, such as those defined by Clapp and Hornberger (1978) and Cosby et al. (1984), to parameterize soil properties (Lawrence and Slater, 2008), usually without consideration of soil property uncertainty (Lawrence and Slater, 2005; Hinzman et al., 1998; Shiklomanov et al., 2007; Koven et al., 2013; Rinke et al., 2008).

Soil property uncertainty is different from many other sources of projection uncertainty (e.g. climate scenario uncertainty) in that uncertainties in soil properties may be reduced by a combination of site characterization (Hinzman et al., 1998) and model calibration (Romanovsky and Osterkamp, 1997; Nicolsky et al., 2009; Jiang et al., 2012; Atchley et al., 2015). Initial steps in that direction have been taken. For example, Romanovsky and Osterkamp (1997) calibrate thermal soil properties using a purely conductive thermal model using measured temperatures at several sites and Nicolsky et al. (2009) perform a sensitivity analysis of a calibration (data assimilation) approach to identify its ability to recover thermal soil properties using a 1-D thermal model and apply the calibration approach to several sites. Atchley

et al. (2015) recently demonstrated an iterative approach for using site characterization data to simultaneously refine thermal hydrology model structure and estimate model parameters. Their approach was applied to the Barrow Environmental Observatory, but could be used at other sites to improve model structure and parameter assignments in the regional or global context.

Recognizing that permafrost projections are sensitive to subsurface model representations and that soil property uncertainties may be reduced through characterization and parameter estimation, a natural next step is to quantify how such activities will impact overall uncertainties in permafrost thaw projections in comparison to other sources of uncertainty. Here we address that question. Specifically, we consider how uncertainties in soil hydrothermal properties propagate to uncertainties in numerical projections of permafrost thaw at a well-characterized site. We go beyond a traditional unconstrained uncertainty quantification and focus on the residual uncertainties that remain after soil parameters have been carefully calibrated to borehole temperature data. The intent of the current work is to develop initial insights into how effective site characterization activities might be at reducing uncertainties associated with soil parameters. We show that with future climate specified and with the advantage of calibration targets from a well-characterized site, significant uncertainties remain in projected ALT and other metrics important for carbon decomposition in the future climate. We show that this residual uncertainty is significant, albeit less than that associated with uncertainties in future climate.

The methodology is described in Sect. 2. A brief description of our thermal hydrology process model is presented in Sect. 3. The generation of the ensemble of calibration-constrained parameter combinations is described in Sect. 4. Permafrost thaw projection metrics are described in Sect. 5. The predictive uncertainty and trends in permafrost thaw projections are presented in Sect. 6. Section 7 presents the comparison of soil property and climate model uncertainty. A correlation analysis identifying the level of dependence between soil parameters and projection metrics is presented in Sect. 8. Conclusions and discussion of the analysis are in Sect. 9.

2 Methodology

We use the Arctic Terrestrial Simulator (ATS) to numerically solve the coupled groundwater flow, thermal, and surface energy balance equations. The uncertainty quantification is performed around a previous calibration by Atchley et al. (2015). Atchley et al. (2015) used 1-D column models representing the dominant microtopographical features (center, rim, and trough of polygonal ground) to calibrate hydro-thermal soil parameters using soil temperatures at the Barrow Environmental Observatory (BEO) measured by the Next Generation Ecosystem Experiments Arctic (NGEE-Arctic) team during calendar year 2013. The calibration considered temperatures measured at 9 depths from 10 to 150 cm.

The calibration was performed in a coupled fashion where each “model run” of the calibration consisted of simulating center, rim, and trough column models with the same soil parameter values for peat and mineral soil. This coupled calibration identifies soil parameters that provide a generalized fit, compromising in a least squares sense to match the data from all three models. An implicit assumption of the coupled calibration is that the soil properties are independent of the microtopography. Atchley et al. (2015) first calibrated subsurface properties using 2 cm deep temperatures measured in 2013 as Dirichlet boundary conditions and temperatures measured at the considered depths as calibration targets. Then an additional surface/subsurface calibration was performed to verify that the surface energy balance model is capable of producing surface temperatures consistent with measurements. The coupled surface/subsurface model allows the use of future climate scenarios as model forcings to drive hydro-thermal permafrost projections.

In order to make projections of hydro-thermal permafrost conditions, we use the surface/subsurface model of Atchley et al. (2015). We use the Community Earth System Model (CESM) (Gent et al., 2011) driven by the Representative Concentration Pathway 8.5 (RCP8.5) greenhouse gas concentration trajectory (Moss et al., 2008) from year 2006 to 2100 as atmospheric forcings for the surface energy balance of the

model. In this way, we hold the climate scenario constant to isolate the effect of soil property uncertainty. RCP8.5 corresponds to a business as usual warming scenario with 8.5 $W m^{-2}$ forcing by 2100.

We generated an ensemble of 1153 calibration-constrained parameter combinations by the Null-Space Monte Carlo (NSMC) method (Doherty, 2004). The NSMC approach samples from insensitive regions of the parameter space (i.e. the null space) determined by an eigenanalysis of parameter sensitivities calculated at the calibration point. Based on analysis of ensemble forward simulations of the calibration year (2013) and a convergence analysis of the 95th confidence band of simulated temperatures, we consider all parameter combinations in the ensemble calibrated and equally consistent with measured temperatures.

Predictive uncertainty of projections is determined by comparison of permafrost metrics at year 2006 and for the last decade of the projections (2091 through 2100). The metrics include (1) ALT, (2) annual thaw depth-duration ($\overline{\mathcal{D}}$), (3) annual mean liquid saturation ($\overline{S}_l$), and (4) a modified Stefan number (S_T) and are described in detail in Sect. 5.

To provide a reference point for the effect and magnitude of soil property uncertainty, we also perform ATS projections forcing the energy balance model with atmospheric projections from CESM, INM-CM4 (INM) (Volodin et al., 2010), BCC-CSM1-1 (BCC) (Ji, 1995), MIROC (Watanabe et al., 2010), CanESM2 (CAN) (Verseghy, 1991), and HadGEM2-CC (HAD) (Jones et al., 2011; Bellouin et al., 2011; Collins et al., 2011) climate models based on RCP8.5 using the calibrated soil parameters from Atchley et al. (2015). Using the calibrated soil parameters in these simulations isolates the effect of structural climate uncertainty. We compare permafrost projection uncertainty due to the NSMC ensemble of soil parameters (hydrothermal soil property uncertainty) and to the variability between climate models (structural climate uncertainty).

The soil property uncertainty in this analysis is parametric and can be considered aleatoric/probabilistic in nature. The climate model uncertainty is epistemic in nature due to a lack of knowledge regarding modeling of atmospheric phenomena. These

distinctions do limit comparisons that can be drawn between these two uncertainties. However, the comparison is relevant for our purposes to provide a frame of reference for soil property uncertainty to one of the other current, primary sources of permafrost thaw uncertainty.

3 Model

We use the ATS computer code to simulate surface/subsurface thermal hydrology processes. ATS is an integrated thermal hydrological code developed specifically for Arctic permafrost applications. It implements the modeling strategy outlined by Painter et al. (2013) using the multiphysics framework Arcos (Coon et al., 2015b) to manage model complexity in process rich simulations such as these. Various components of ATS have already been described elsewhere, therefore, only a brief summary is provided here.

In the subsurface, the ATS solves nonlinear conservation equations for water and energy, using a three-phase (air-water-ice), single-component representation (Karra et al., 2014), which is a simplification of a more general two-component (water and representative gas phase) model (Painter, 2011). A recently developed constitutive model (Painter and Karra, 2014) is used to partition water between ice and liquid phases in unsaturated or saturated conditions. The partitioning model relates unfrozen water content below the nominal freezing point to the unfrozen soil moisture characteristic curve, thus avoiding empirical freezing curves. The model has been successfully compared to a variety of laboratory experiments on freezing soils (Painter and Karra, 2014; Karra et al., 2014; Painter, 2011). Surface boundary conditions use a "fill and spill approximation", where we allow up to 4 cm of water to pond on the surface; all additional ponded water may run off the domain. The surface and subsurface thermal hydrology systems are coupled using continuity of pressure, mass flux, temperature, and energy flux, in a thermal extension of the coupling strategy presented in Coon et al. (2015a). Additionally, we use a surface energy

balance (Hinzman et al., 1998; Ling and Zhang, 2004; Atchley et al., 2015) in which surface latent and sensible heat, incoming and outgoing radiation, and conducted heat terms, along with incoming precipitation and outgoing evaporation are tracked. Finally, a dynamic, single-layer snow model is incorporated for tracking snow aging and consolidation, with resulting effects on albedo and melt (Atchley et al., 2015). Not represented within this system are carbon cycle and vegetation processes, including long-term changes of peat composition, variability in peat thickness, and evolving microtopography due to degradation of ice wedges.

The subsurface domain is represented by a 2 cm layer of moss, followed by a 10 cm layer of peat, and approximately 50 m mineral soil layer. The required climate forcings for the ATS models are precipitation of snow and rain, air temperature, wind speed, relative humidity, and incoming short and longwave radiation.

4 Creation of ensemble of soil parameter combinations

In order to determine the effect that calibration-constrained soil property uncertainty can have on long term projections of permafrost conditions, we performed an uncertainty quantification around the calibrated soil parameters of Atchley et al. (2015). The strategy involved identifying a representative set of parameter combinations that all produce simulated temperatures that are consistent with observed temperatures. We use Null-Space Monte Carlo (NSMC) (Tonkin and Doherty, 2009), a form of calibration-constrained Monte Carlo, to accomplish this goal. NSMC was selected based on its sampling economy given the computational burden of the simulations involved.

A subset of the 16 soil parameters from the calibration of Atchley et al. (2015) are included here and presented in Table 1. The top pressures of the center and trough profiles from the calibration (parameters *topprescr* and *topprestrg* in Atchley et al., 2015) are not included here as these are internally calculated in the surface/subsurface ATS model. The van Genuchten water retention parameters (α_{vgpeat}, α_{vgmin}, m_{vgpeat}, m_{vgmin} in Atchley et al., 2015) are not included either as they were found to significantly

exceed their physical boundaries during NSMC sampling. This is an indication that these are highly insensitive parameters and do not significantly effect simulated temperatures. This may be explained by the fact that these parameters control the shape of the water retention curve, but that this influences thermal properties of the soil only for a limited time near freeze-up or thaw.

This leaves the 10 soil parameters listed in Table 1. The parameters $\Theta_{\mathrm{r,peat}}$ and $\Theta_{\mathrm{r,min}}$ are van Genuchten soil moisture characteristic residual saturations (Van Genuchten, 1980). K_{peat} and K_{min} are thermal conductivities for peat organic matter and mineral grains within the soil layers. These are not bulk thermal conducitivities for the soil layers, but are used in their calculation. $A_{\mathrm{peat,\,fr}}$, $A_{\mathrm{peat,\,un}}$, $A_{\mathrm{peat,\,fr}}$, and $A_{\mathrm{peat,\,un}}$ are emperical exponents describing the dependence of frozen (fr) and unfrozen (un) Kersten numbers (i.e. ratios of partially to fully saturated thermal conductivities) to ice and liquid saturation states, respectively (Painter, 2011). Bulk thermal conductivities for peat and mineral soil layers are calculated within ATS using the Material Component model defined by Atchley et al. (2015) with the parameters listed in Table 1. The minimum and maximum parameter boundaries are modified from the calibration for the NSMC sampling (the parameter ranges are reduced in most cases) to physical limits identified through literature review and field observations from the BEO (Hinzman et al., 1991, 1998; Lawrence and Slater, 2008; Letts et al., 2000; Beringer et al., 2001; Overduin et al., 2006; O'Donnell et al., 2009; Quinton et al., 2000; Nicolsky et al., 2009; Zhang et al., 2010).

To a lesser degree, other parameters were also found to exceed their physical boundaries during NSMC sampling. Therefore, we used the intersection of the null space and parameter boundaries as our criterion to accept samples. The generation of 20 000 samples within the null space resulted in 1153 samples within the parameter boundaries. Samples outside of the parameter boundaries were discarded.

Figure 1 presents histograms while Fig. 2 presents paired plots of the NSMC ensemble soil parameters. In the matrix of plots in Fig. 2, parameter histograms are plotted along the diagonal (also presented in greater detail in Fig. 1), paired scatterplots

in the lower triangle, and Pearson correlation coefficients are presented in the upper triangle. In Fig. 1, it is apparent that K_{peat} followed by $A_{peat,\,un}$ are the most constrained parameter by the NSMC analysis. The rest of the parameters span significant portions of their range. This indicates that their are many combinations of parameters that result in calibrated temperatures. Many of the histograms are seen to butt up against their boundaries, indicating that these are parameters where the extent of the null space exceeds their range.

The correlations imposed by the NSMC sampling are evident by inspecting the Pearson correlation coefficients and scatterplots in Fig. 2. The strong correlations that are present are a result of a balancing act between parameters to achieve a least squares fit to measured temperatures. For example, the relatively strong negative correlation between K_{peat} and K_{min} (correlation of −0.81) is due to the fact that deeper temperatures in the soil profiles are controlled by the effective thermal conductivity. Therefore, there are numerous (negatively correlated) combinations of K_{peat} and K_{min} that produce similar effective thermal conductivities resulting in good matches to measured temperatures. Many other correlated parameter pairs are also apparent, most with significantly lower correlations. There are also many uncorrelated parameter pairs (e.g. ϕ_{peat} and K_{peat}) indicating a complete lack of interaction between the parameter pairs. The following analysis of permafrost projection uncertainty is conditional on the NSMC correlations presented here, and any conclusions take these correlations into account. References to Fig. 2 are made in the following sections explaining some of the impacts of these correlations.

The range in RMSE values is from around 0.55 to 0.65 °C. The accuracy of the temperature probes are ±0.02 °C. Therefore, the percentage of the RMSE that may be attributable to measurement imprecision is around 2–3 %.

Figure 3 presents the 95 % confidence band of temperatures for the NSMC ensemble. Figure 4 presents the convergence analysis for the NSMC ensemble based on the confidence band inclusion ratio (i.e. the ratio of measured temperatures within the 95th% confidence band of the ensemble simulated temperatures). The relatively

stable confidence band inclusion ratio after around 800 ensemble members indicates that the ensemble has converged and that more samples are not necessary. The measured temperatures are within the 95 % confidence band 79 % of the time for the center, 59 % for the rim, 46 % for the trough, and 61 % overall. The primary causes of these discrepencies are due to difficulties in capturing trends that are not purely random. The low values are primarily due to the 95 % confidence band missing measured values at deep measurements apparent in Figs. A1–A3 in Appendix . A lack of overlap is apparent during thawing (around day of year 150) and freeze-up (around day of year 320), and is particularly evident in the rim profile in Fig. 3. Many physical processes may be leading to this result. For one, the exposed sides of the rim and subsequent lateral heat flow are not explicitly modeled and may at least partially explain the discrepency. During the thaw, a lack of advective transport of heat by liquid water through the pore space created by sublimation during the winter (not included in the model) may result in warmer measured temperatures.

NSMC conventionally involves a recalibration step, where a few Levenberg-Marquardt iterations are applied to each NSMC sample, often using existing sensitivities from the calibration point. Based on the RMSE values of the ensemble and the percentages of measured temperatures within the 95 % confidence band, we consider all the unmodified NSMC samples to be calibrated and do not apply this step. These observations also led to the assumption that all NSMC samples are equally consistent with measured temperatures as opposed to using a weighting scheme.

An initial ensemble created using Latin Hypercube Sampling with 1000 samples postprocessed to include parameter combinations with RMSE's below various thresholds indicated that to achieve a convergent ensemble using Latin Hypercube Sampling would be computational prohibitive. An additional NSMC analysis was performed with a more restrictive null space (only 2 eigenvectors out of 10 included in the null space). This ensemble did not require postprocessing based on RMSE, since all the RMSE values were deemed sufficiently small. This analysis resulted in over-correlated parameters. We therefore chose a loosely constrained NSMC (5 out

of 10 eigenvectors included in the null-space) excluding samples with RMSE greater than 0.65 °C. We considered other RMSE cutoffs, but selected 0.65 °C based on compromising between increasing the confidence band inclusion ratio and ensuring that simulated temperatures for 2013 were as consistent near the active layer base as possible across the ensemble. ALT in 2013 was around 40 cm (refer to Figs. A1–A3).

The projection simulations took on the order of several hours (∼ 2–4 h) on a Linux cluster with 3.2 GHz processors. We used the Model Analysis ToolKit (MATK) Python module (http://matk.lanl.gov) to facilitate the concurrent execution of the ensemble of ATS models on high performance computing clusters.

5 Permafrost metrics

5.1 Active layer thickness (ALT)

Permafrost is traditionally defined as the region of the subsurface that remains at or below 0 °C for two or more years. The ALT defined that way would be the minimum of the maximum annual thaw depth over each two year moving window. We use a less arbitrary definition for the ALT here as the annual maximum thaw depth, similar to Koven et al. (2011). Given the discrete nature of our mesh, and the nonlinear nature of vertical soil temperature profiles near 0 °C, we determine ALT as the bottom of the deepest thawed mesh cell (temperature above 0 °C) for the year.

5.2 Annual thaw depth-duration ($\overline{\mathcal{D}}$)

ALT controls the amount of organic carbon experiencing thaw and thus microbially induced decomposition during a year. Because ALT is defined as the maximum thaw depth, it does not include information on duration of thaw. To quantify increasing duration of thaw in future climate as well as increasing depth, a new metric is introduced

here: the mean annual thaw depth $\overline{\mathcal{D}}$, defined as

$$\overline{\mathcal{D}} = \frac{1}{365}\int\int H(T(z,t))\mathrm{d}z\mathrm{d}t \tag{1}$$

where H is the heavyside function (1 if $T(z,t)$ is above 0 °C, 0 otherwise), z is depth in meters, and t is time in days. The fraction on the right side of Eq. (1) normalizes the metric by the 365 days in a year. We express $\overline{\mathcal{D}}$ with units of $\mathrm{m}^3\,\mathrm{m}^{-2}$ to indicate that this metric defines the volume of thawed soil per unit area. Of course, this can be reduced to simply meters, however, it must be recognized that the metric is averaged over the entire year including while the soil column is completely frozen. $\overline{\mathcal{D}}$ is a rough proxy for the potential for soil organic matter decomposition. It merges the amount of unfrozen soil and duration that soil is above freezing for a given year. It is noted that, while the annual amount of decomposition is likely correlated with $\overline{\mathcal{D}}$, the two quantities are not directly proportional because soil temperature and moisture will also change and affect the decomposition rates in future climates. In addition, the soil organic matter content in soils generally decreases with depth, which is not accounted for in the $\overline{\mathcal{D}}$ metric. Nevertheless, uncertainty in $\overline{\mathcal{D}}$ is of interest as it is an important control on uncertainty in future decomposition rates.

5.3 Annual mean liquid saturation ($\overline{S}_\mathrm{l}$)

The annual mean liquid saturation $\overline{S}_\mathrm{l}$ is defined as

$$\overline{S}_\mathrm{l} = \frac{\int\int H(T(z,t))S_\mathrm{l}(z,t)\mathrm{d}z\mathrm{d}t}{\int\int H(T(z,t))\mathrm{d}z\mathrm{d}t}. \tag{2}$$

$\overline{S}_\mathrm{l}$ quantifies the spatially and temporally averaged liquid saturation in the unfrozen soil for a given year. Note that the denominator in Eq. (2) is the annual thaw depth-duration

metric $\overline{\mathcal{D}}$ from above, except without dividing by 365. While frozen soil (i.e. soil below 0 °C) in our models contain a residual liquid saturation, this is not included in $\overline{S}_{\mathrm{l}}$ (refer to Eq. 2). Liquid saturation within the active layer is of interest because of its control on decomposition rates. In particular, decomposition may be slower in dry conditions, and oxygen limitations in saturated or nearly saturated conditions may cause methane production to be favored over CO_2 production. Therefore, $\overline{S}_{\mathrm{l}}$ provides an indication of the potential rate of decomposition as well as an indication of the chemical form of the resulting greenhouse gas produced in the active layer.

5.4 Stefan number (S_T)

We propose an extension of the Stefan number from the form in Kurylyk et al. (2014) to one that incorporates intra-annual temporal changes and stratified soil properties. The Stefan number is the ratio of subsurface sensible to latent heat. In the current context, this refers to the amount of subsurface heat exchange that results in a change in temperature vs. the amount that is consumed in the isothermal conversion of ice to liquid water. In its most basic form, the Stefan number is defined as

$$S_T = \frac{c_{\mathrm{b}} \Delta T}{L_{\mathrm{f}}}. \tag{3}$$

where c_{b} is the bulk specific heat of the material and L_{f} is the latent heat of fusion of water (334 000 J kg^{-1}). Kurylyk et al. (2014) define the Stefan number for the permafrost problem as

$$S_T = \frac{c_{\mathrm{b}} \rho_{\mathrm{b}} (T_{\mathrm{s}} - T_{\mathrm{f}})}{S_{\mathrm{wf}} \rho_{\mathrm{w}} \phi L_{\mathrm{f}}} \tag{4}$$

where ρ_{b} is the density of the thawed zone, T_{s} is the surface temperature, T_{f} is the temperature of freezing or thawing soil (taken as 0 °C), S_{wf} is the liquid saturation in the thawed zone that was frozen, and ρ_{w} is the density of liquid water. Kurylyk et al.

(2014) use this definition to evaluate the thermal regime of analytical solutions of soil thaw. We expand this definition here to include the increased detail available in our numerical simulations as

$$S_T = \frac{\int\int c_{\mathrm{b}}(z) \rho_{\mathrm{b}}(z)\, H\left(\frac{\mathrm{d}T}{\mathrm{d}t}\right) \frac{\mathrm{d}T}{\mathrm{d}t} \mathrm{d}z\mathrm{d}t}{\rho_{\mathrm{ice}} L_{\mathrm{f}} \int\int H\left(-\frac{\mathrm{d}S_{\mathrm{ice}}}{\mathrm{d}t}\right)\left(-\frac{\mathrm{d}S_{\mathrm{ice}}}{\mathrm{d}t}\right) \phi(z) \mathrm{d}z\mathrm{d}t} \tag{5}$$

where S_{ice} is ice saturation. The integrations are performed over the entire year (i.e. from 1 January through 31 December). Equation (5) expands on Eq. (4) to allow the consideration of details of transient heating and cooling throughout the year and stratified hydrothermal soil properties within the soil profile.

6 Permafrost thaw projection uncertainty

Figure 5 present boxplots of permafrost metrics for the first year (2006) and the last decade (2091–2100) of the projections. Individual boxplots for each year present the intra-annual predictive uncertainty, while comparisons between boxplots for each metric indicate the inter-annual variability of the projections for the specified climate scenario. We present the first year as an indication of the intra-annual uncertainty at the beginning of the projections.

Boxplots of ALT are shown in Fig. 5a. The median ALT increased from approximately 30 cm in 2006 to nearly 0.9 m by the end of the century. The intra-annual uncertainty in ALT also increases significantly from the beginning to later years of the projections. The intra-annual variability of ALT projections is dependent on climate, as warmer years (e.g. 2094) have greater ALT and larger uncertainty than cooler years. This is apparent in Fig. 6 where the ensemble thaw depth statistics (median and 95 % confidence band) and CESM8.5 air temperature times series are plotted together for comparison.

Boxplots of annual thaw depth-duration ($\overline{\mathcal{D}}$) are presented in Fig. 5b. The intra-annual uncertainty in $\overline{\mathcal{D}}$ during the last decade of the projections is significantly greater than

for the first year (2006). As expected, the inter-annual trends in $\overline{\mathcal{D}}$ and ALT are similar. Also, the uncertainty of $\overline{\mathcal{D}}$ is relatively larger during warmer years than cooler years, similar to ALT.

Boxplots of the annual mean liquid saturation ($\overline{S}_l$) are presented in Fig. 5c. The intra-annual uncertainty in $\overline{S}_l$ actually decreases slightly from the first year to the last decade. Also, in general, the last decade is slightly wetter than 2006, but only marginally so. Therefore, this hydrothermal analysis does not indicate that the partitioning of carbon decomposition between CO_2 and CH_4 will change significantly as permafrost thaws. However, other factors affecting carbon decomposition not considered here could affect the partitioning of carbon decomposition end products.

Boxplots of the Stefan number (S_T) are presented in Fig. 5d. In 2006 the soil profiles for the majority of the ensemble are latent heat dominated. However, some Stefan numbers are greater than 1, with values ranging from around 0.3 to 1.4 (from around 3 times the latent heat as sensible heat to 1.4 times the sensible as latent heat). However, by the last decade, nearly all Stefan numbers are 0.2 or less (at least 5 times as much, and up to 20 times as much latent heat as sensible heat). This indicates a fundamental change in the way that the active layer processes energy between the beginning and later years of the projections. The thermal regime of the active layer becomes significantly more dominated by latent heat during the projections. The amount of energy that is utilized in creating a temperature gradient in the soil profile becomes proportionately smaller compared to the amount of energy consumed in the isothermal melting of ice. This is at least partially due to the approximately 3 times increase in the quantity of ice that is melted during later years of the projections. Perhaps the most significant result of this change is the temperature regime of the underlying permafrost in decreased seasonal temperature variations and their depth of penetration. Intra-annual uncertainty appears to decrease from 2006 compared to the last decade, but this is likely due to the Stefan number approaching its lower limit.

To further illustrate intra-annual uncertainty of the ALT projections, temperature profiles at the time of ALT for year 2100 are presented in Fig. 7. Summary statistics

(median and 5th and 95th percentiles) for 2006 are presented for reference. The discrete surface temperatures categorized by day of year (colors) reflect the fact that the surface temperature is highly dependent on the climate/air temperature, which is the same for all projections. The increase in median ALT from around 30 cm to around 0.9 m from 2006 to 2100 is also apparent in this figure. The difference in the temperature regime within the profile is apparent in these figures as well by the curve near the surface in most of the profiles in 2100 compared to 2006. This indicates that as the climate warms and the day of year when ALT occurs becomes later in the year (day of year ALT occurs in 2006 projections is from 246 to 260), the surface temperature at that time will be cooler. This increase in lag time from the surface temperature to the active layer base is a result of the thermal wave traveling a greater distance to reach the permafrost. This may also be due to relative changes in the temperature gradient within the active layer and the permafrost as the ALT increases leading to delayed freeze from below.

Figure 8 shows similar plots to Fig. 7, but in this case, statistical measures of the ensemble are plotted. Statistical representation of the temperature profiles in Fig. 7 are plotted in Fig. 8a, along with bulk thermal conductivity (Fig. 8b) and ice (Fig. 8c), liquid (Fig. 8d), and gas (Fig. 8e) saturation profiles when ALT occurs in 2006 and 2100. The variation in thermal conductivity and saturation states further illustrates the intra-annual projection uncertainty due solely to soil properties. Substantial shifts in intra-annual uncertainty are also apparent from 2006 to 2100. In Fig. 8a, it is apparent that the thermal conductivity in the soil profile decreases from 2006 to 2100 due to the loss of the more thermally conductive ice from the profile, thereby inhibiting the propagation of the thermal wave. The deepening of the permafrost table is apparent in Fig. 8c as a deepening of the ice saturated region. Note that liquid saturations for mineral soil remain at its residual values below 0 °C and that residual liquid saturations ($\Theta_{r,peat}$ and $\Theta_{r,min}$) are variable parameters within the uncertainty quantification (refer to Table 1). As a result, the ice saturation within the permafrost region is variable within the ensemble. In Fig. 8d and e, it is apparent that the liquid and gas saturations both increase as

ice is converted to liquid and void space becomes available with the deepening of the permafrost table.

7 Comparison to climate model structural uncertainty

In this section, we provide a frame of reference to the effect of soil property uncertainty on permafrost thaw projections by comparison to the uncertainty currently present in climate models. Figure 9 presents histograms of projection metrics collected from each ensemble sample for years 2091 through 2100 (a total of 11 530 values, i.e. 1153 samples × 10 years). This combines the intra-annual uncertainty for the last decade of the projections. The 95 % confidence band of the calibration-constrained ensemble for each metric is indicated by dashed vertical lines in each plot. Below the histograms are the values obtained using atmospheric forcing data from CESM, INM, BCC, MIROC, CAN, and HAD climate models to drive the ATS models with the calibrated soil parameters for the same years, 10 values each. BCC has only 9 values as we could only obtain its data through year 2099. These values provide a sampling of current climate model structural uncertainty due to varying assumptions and numerical representations of atmospheric phenomena.

Note that the CESM values lie within the support of the calibration-constrained ensemble histograms in all cases. This is expected since the calibration-constrained ensemble is forced using the CESM scenario. Similarly, the supports of calibration-constrained ensemble histograms for other climate scenarios would be expected to encompass the calibrated soil parameter values (circles in Fig. 9) as well. This indicates that different climate scenarios will result in different magnitudes of projection uncertainty due to soil property uncertainty. For example, if the calibration-constrained ensemble was simulated using MIROC, the magnitude of the projection uncertainty of $\overline{\mathcal{D}}$ (Fig. 9b) could be as much as 4–5 times larger than for CESM. This indicates the interactive effect that soil property and structural climate model uncertainties have on projection uncertainty and that these forms of uncertainty are not easily decoupled.

These plots present the magnitude of projection uncertainty due to only soil property uncertainty based on CESM atmospheric projections (histograms) and to only structural climate model uncertainty (circles). By comparing the ensemble 95 % confidence bands for the metrics to the range of values across the climate models, it is apparent that structural climate model uncertainty has a greater impact on projection uncertainty than soil property uncertianty. The ratios of the ensemble 95 % confidence band width and the range between the minimum and maximum values for climate models are 26 % for ALT, 9 % for $\overline{\mathcal{D}}$, 45 % for $\overline{S}_{\mathrm{I}}$, and 80 % for S_T. As explained above, if a different climate model had been used for the ensemble calculations, these percentages would be different.

8 Dependence of permafrost projections on soil parameters

Figure 10 presents paired plots of calibration-constrained projections for year 2100. The diagonals are projection histograms, the lower triangle contains paired scatterplots, and the upper triangle contains the Pearson correlation coefficients between matrix pairs. The samples are discrete in ALT due to the mesh discretization. The mesh cell thickness increases with depth, and the active layer is determined as the depth to the bottom of the deepest unfrozen cell (i.e. with a temperature above 0 °C).

From this figure, it is apparent that all the metrics are positively correlated. The correlation between ALT and $\overline{\mathcal{D}}$ is expected given the definition of $\overline{\mathcal{D}}$ as a metric defining the quantity and duration of unfrozen soil. The correlation of $\overline{S}_{\mathrm{I}}$ to ALT is a result of the deeper portions of the thicker ALT scenarios having slightly increased levels of saturation, which is apparent in the liquid saturation statistical profiles in Fig. 8d for year 2100. The correlation between $\overline{\mathcal{D}}$ and $\overline{S}_{\mathrm{I}}$ can be explained by a similar argument. Increased levels of saturation lead to higher bulk thermal conductivy of the mineral soil layer, resulting in thicker ALT and larger $\overline{\mathcal{D}}$ due to increased energy flux. Correlations between S_T and the other projection metrics indicate that as ALT increases, resulting

in increased annual thaw depth-duration $\overline{\mathcal{D}}$ and annual mean liquid saturation $\overline{S}_l$, the system becomes increasingly latent heat dominated. This is due to the fact that more energy is required to thaw greater depths of frozen soil each year.

Figures 11–14 explore correlations between the calibration-constrained parameters and projected metrics. These figures plot scatterplots between hydro-thermal soil parameters and projection metrics for year 2100. The discrete nature of the samples with respect to ALT mentioned above due to the mesh discretization is also apparent in Fig. 11. Pearson correlation coefficients for each soil parameter/projection metric pair are presented on each scatterplot. The points are colored by $\overline{\mathcal{D}}$ in Fig. 11 and by ALT in Figs. 12–14 to further illustrate the correlations between metrics already presented in Fig. 10. Peat parameters are presented along the left column and mineral soil parameters along the right column of each figure.

Some strong correlations are apparent in Figs. 11–14 with coefficients greater that 0.9. Many of these correlations confirm our qualitative understanding of the model. It is apparent that in many cases projection metrics have stronger dependencies on the mineral soil porosity (ϕ_{min}) and residual saturation ($\Theta_{\mathrm{r,min}}$) parameters compared to the corresponding peat parameters (ϕ_{peat} and $\Theta_{\mathrm{r,peat}}$). Dependence on the other parameters is less predictable. For example, decreasing mineral soil porosity (ϕ_{min}) increases the bulk thermal conductivity of the mineral soil due to the relatively large thermal conductivity of the mineral soil grains, leading to larger ALT (top right plot in Fig. 11).

We determine linear dependency coefficients of projection metrics to calibration-constrained parameters using ordinary least squares. We limit the analysis to soil parameter/projection metrics exibiting moderate to strong correlation ($|\rho| > 0.7$). Table 2 presents the intercept and slope coefficients from the analysis, along with their 95 % confidence intervals. All coefficients in Table 2 are significant at the 1 % level. The coefficient of determination (R^2) is presented indicating the portion of the variance explained by the regression for each case. Note that since we use ordinary least squares including an intercept, the R^2 is simply the square of the correlation

coefficients (ρ) presented in Figs. 11–14. Calibration-constrained parameters not included in Table 2 resulted in regressions with R^2 less than 0.5.

The slope coefficients are emphasized in bold in the table since these describe the first-order dependence of projection metrics on the calibration-constrained parameters. The slope coefficients describe the change in ALT given a unit change in the calibration-constrained parameter. For example, if ϕ_{min} increases by 0.1, we would estimate that ALT will decrease by around 0.14 m. These coefficients can be useful in gaging the impact of soil parameter changes on projection metrics.

9 Discussion and conclusions

In summary, we extended previous calibration and model refinement work (Atchley et al., 2015) to quantify post-calibration uncertainty in soil properties and the impact of that uncertainty on projections of permafrost thaw. Using a model with parameters calibrated against data from the BEO, driving the NSMC ensemble of models using the CESM climate model in the RCP8.5 scenario, and comparing against other climate models in the RCP8.5 scenario, the following conclusions can be made:

- The median ALT and annual thaw depth-duration ($\overline{\mathcal{D}}$) of the calibration-constrained ensemble increase by around a factor of 3 by the end of the century.
- The effect of soil property uncertainty based on CESM atmospheric forcings is approximately 26 % of the uncertainty caused by climate model structural uncertainty for ALT, 9 % for $\overline{\mathcal{D}}$, 45 % for $\overline{S}_l$, and 80 % for Stefan number.
- Intra-annual uncertainty of ALT and $\overline{\mathcal{D}}$ due to soil property uncertainty increase significantly from the first year to the last decade of the projections
- Intra-annual uncertainty of soil moisture content due to soil property uncertainty is not significantly changed by the end of the century.

– Intra-annual uncertainty of the Stefan number due to soil property uncertainty decreases, but this is at least partially due to this metric approaching its lower boundary in the last decade.

– The active layer moves to an increasingly latent heat dominated system due to larger quantities of frozen ground thawed each year.

– ALT, $\overline{\mathcal{D}}$, and S_T are highly dependent on $\phi_{\min}$, while $\overline{S}_{\mathrm{l}}$ is highly dependent on $\Theta_{\mathrm{r,min}}$ and moderately dependent on $\Theta_{\mathrm{r,peat}}$.

Efforts to quantify the relative roles of subsurface vs. climate and scenario uncertainty have only recently begun. We found that the effect of soil property uncertainties can be reduced to levels lower than the uncertainty generated by uncertainties in climate model structure through a process of calibration to field observations, model structural refinement (Atchley et al., 2015), and calibration-constrained uncertainty analysis. However, we had the advantage of data from an unusually well-characterized site, which suggests that the residual uncertainty identified here is close to a practical limit.

The quantitative results shown here are specific to the site, available data, RCP trajectory assumption, and climate model. Nevertheless, the approach presented here is anticipated to be useful for understanding the impact that additional data collection might have on reducing uncertainty associated with other high-latitude permafrost sites. Potential directions for future work include the investigation on the impact that longer data streams and other types of observation might have on reducing uncertainties. In particular, the calibration against borehole temperature data was uninformative of certain water retention properties of the soils (van Genuchten α and m parameters). Therefore, co-located measurements of soil moisture would be useful to help constrain those parameters. Moreover, given the known spatial variability in soil properties across the pan-Arctic (Hinzman et al., 1998; Rawlins et al., 2013), calibration-constrained soil property uncertainty across larger spatial scales warrants further investigations.

Appendix A

Figures A1–A3 present the 95th confidence band for NSMC ensemble temperatures during the calibration year for all depths. These figures present the complete data set from which Fig. 3 was drawn, which presents the 40 cm depth values only (near the ALT in 2013).

Acknowledgements. This research was supported by the Next-Generation Ecosystem Experiments Arctic (NGEE-Arctic) project (DOE ERKP757) funded by the Office of Biological and Environmental Research in the US Department of Energy Office of Science and Los Alamos National Laboratory's Laboratory Directed Research and Development (LDRD) Arctic project (LDRD201200068DR).

References

Atchley, A. L., Painter, S. L., Harp, D. R., Coon, E. T., Wilson, C. J., Liljedahl, A. K., and Romanovsky, V. E.: Using field observations to inform thermal hydrology models of permafrost dynamics with ATS (v0.83), Geosci. Model Dev. Discuss., 8, 3235–3292, doi:10.5194/gmdd-8-3235-2015, 2015. 3354, 3356, 3357, 3359, 3360, 3372, 3373

Beringer, J., Lynch, A. H., Chapin III, F. S., Mack, M., and Bonan, G. B.: The representation of arctic soils in the land surface model: the importance of mosses, J. Climate, 14, 3324–3335, 2001. 3354, 3360

Chadburn, S. E., Burke, E. J., Essery, R. L. H., Boike, J., Langer, M., Heikenfeld, M., Cox, P. M., and Friedlingstein, P.: Impact of model developments on present and future simulations of permafrost in a global land-surface model, The Cryosphere Discuss., 9, 1965–2012, doi:10.5194/tcd-9-1965-2015, 2015. 3354

Clapp, R. B. and Hornberger, G. M.: Empirical equations for some soil hydraulic properties, Water Resour. Res., 14, 601–604, 1978. 3354

Collins, W. J., Bellouin, N., Doutriaux-Boucher, M., Gedney, N., Halloran, P., Hinton, T., Hughes, J., Jones, C. D., Joshi, M., Liddicoat, S., Martin, G., O'Connor, F., Rae, J., Senior, C., Sitch, S., Totterdell, I., Wiltshire, A., and Woodward, S.: Development and evaluation of an

Earth-System model – HadGEM2, Geosci. Model Dev., 4, 1051–1075, doi:10.5194/gmd-4-1051-2011, 2011. 3357
Coon, E., Moulton, J., Berndt, M., Manzini, G., Garimella, R., Lipnikov, K., and Painter, S.: Coupled surface and subsurface hydrologic flow using mimetic finite differences, Adv. Water Resour., in review, 2015a. 3358
Coon, E. T., Moulton, J. D., and Painter, S. L.: Managing complexity in land surface and near-surface process models, Environ. Modell. Softw., under review, 2015b. 3358
Cosby, B., Hornberger, G., Clapp, R., and Ginn, T.: A statistical exploration of the relationships of soil moisture characteristics to the physical properties of soils, Water Resour. Res., 20, 682–690, 1984. 3354
Doherty, J.: Model-Independent Parameter Estimation, User Manual, Watermark Numerical Computing, Australia, 2004. 3357
Gent, P. R., Danabasoglu, G., Donner, L. J., Holland, M. M., Hunke, E. C., Jayne, S. R., Lawrence, D. M., Neale, R. B., Rasch, P. J., Vertenstein, M., Worley, P. H., Yang, Z.-L., and Zhang, M.: The community climate system model version 4, J. Climate, 24, 4973–4991, 2011. 3356
Hinzman, L., Kane, D., Gieck, R., and Everett, K.: Hydrologic and thermal properties of the active layer in the Alaskan Arctic, Cold Reg. Sci. Technol., 19, 95–110, 1991. 3354, 3360
Hinzman, L. D., Goering, D. J., and Kane, D. L.: A distributed thermal model for calculating soil temperature profiles and depth of thaw in permafrost regions, J. Geophys. Res.-Atmos., 103, 28975–28991, 1998. 3354, 3359, 3360, 3373
Hinzman, L. D., Bettez, N., Chapin, F., Dyurgerov, M., Fastie, C., Griffith, D., Hope, A., Huntington, H., Jensen, A., Kane, D., Kofinas, G., Lynch, A., Lloyd, A., McGuire, A. D., Nelson, F. E., Osterkamp, T., Oechel, W. C., Racine, C., Romanovsky, V. E., Schimel, J., Stow, D., Sturm, M., Tweedie, C. E., Vourlitis, G., Walker, M., Webber, P. J., Welker, J., Winker, K., and Yoshikawa, K.: Evidence and implications of recent climate change in terrestrial regions of the Arctic, in: AGU Fall Meeting Abstracts, vol. 1, American Geophysical Union, San Francisco, USA, p. 0010, 2002. 3353
Ji, J.: A climate-vegetation interaction model: simulating physical and biological processes at the surface, J. Biogeogr., 22, 445–451, 1995. 3357
Jiang, Y., Zhuang, Q., and O'Donnell, J. A.: Modeling thermal dynamics of active layer soils and near-surface permafrost using a fully coupled water and heat transport model, J. Geophys. Res., 117, D11110, doi:10.1029/2012JD017512, 2012. 3354

Jones, C. D., Hughes, J. K., Bellouin, N., Hardiman, S. C., Jones, G. S., Knight, J., Liddicoat, S., O'Connor, F. M., Andres, R. J., Bell, C., Boo, K.-O., Bozzo, A., Butchart, N., Cadule, P., Corbin, K. D., Doutriaux-Boucher, M., Friedlingstein, P., Gornall, J., Gray, L., Halloran, P. R., Hurtt, G., Ingram, W. J., Lamarque, J.-F., Law, R. M., Meinshausen, M., Osprey, S., Palin, E. J., Parsons Chini, L., Raddatz, T., Sanderson, M. G., Sellar, A. A., Schurer, A., Valdes, P., Wood, N., Woodward, S., Yoshioka, M., and Zerroukat, M.: The HadGEM2-ES implementation of CMIP5 centennial simulations, Geosci. Model Dev., 4, 543–570, doi:10.5194/gmd-4-543-2011, 2011. 3357
Jones, P. D. and Moberg, A.: Hemispheric and large-scale surface air temperature variations: an extensive revision and an update to 2001, J. Climate, 16, 206–223, 2003. 3353
Karra, S., Painter, S. L., and Lichtner, P. C.: Three-phase numerical model for subsurface hydrology in permafrost-affected regions (PFLOTRAN-ICE v1.0), The Cryosphere, 8, 1935–1950, doi:10.5194/tc-8-1935-2014, 2014. 3358
Koven, C. D., Ringeval, B., Friedlingstein, P., Ciais, P., Cadule, P., Khvorostyanov, D., Krinner, G., and Tarnocai, C.: Permafrost carbon-climate feedbacks accelerate global warming, P. Natl. Acad. Sci. USA, 108, 14769–14774, 2011. 3353, 3363
Koven, C. D., Riley, W. J., and Stern, A.: Analysis of permafrost thermal dynamics and response to climate change in the CMIP5 Earth system models, J. Climate, 26, 1877–1900, 2013. 3353, 3354
Kurylyk, B. L., McKenzie, J. M., MacQuarrie, K. T. B., and Voss, C. I.: Analytical solutions for benchmarking cold regions subsurface water flow and energy transport models: one-dimensional soil thaw with conduction and advection, Adv. Water Resour., 70, 172–184, doi:10.1016/j.advwatres.2014.05.005, 2014. 3354, 3365
Langer, M., Westermann, S., Heikenfeld, M., Dorn, W., and Boike, J.: Satellite-based modeling of permafrost temperatures in a tundra lowland landscape, Remote Sens. Environ., 135, 12–24, 2013. 3354
Lawrence, D. M. and Slater, A. G.: A projection of severe near-surface permafrost degradation during the 21st century, Geophys. Res. Lett., 32, L24401, doi:10.1029/2005GL025080, 2005. 3354
Lawrence, D. M. and Slater, A. G.: Incorporating organic soil into a global climate model, Clim. Dynam., 30, 145–160, 2008. 3354, 3360

Letts, M. G., Roulet, N. T., Comer, N. T., Skarupa, M. R., and Verseghy, D. L.: Parametrization of peatland hydraulic properties for the Canadian land surface scheme, Atmos. Ocean, 38, 141–160, 2000. 3354, 3360

Ling, F. and Zhang, T.: A numerical model for surface energy balance and thermal regime of the active layer and permafrost containing unfrozen water, Cold Reg. Sci. Technol., 38, 1–15, 2004. 3359

Moss, R. H., Babiker, M., Brinkman, S., Calvo, E., Carter, T., Edmonds, J. A., Elgizouli, I., Emori, S., Lin, E., Hibbard, K., Jones, R., Kainuma, M., Kelleher, J., Lamarque, J. F., Manning, M., Matthews, B., Meehl, J., Meyer, L., Mitchell, J., Nakicenovic, N., O'Neill, B., Pichs, R., Riahi, K., Rose, S., Runci, P. J., Stouffer, R., VanVuuren, D., Weyant, J., Wilbanks, T., van Ypersele, J. P., and Zurek, M.: Towards new scenarios for analysis of emissions, climate change, impacts, and response strategies, intergovernmental Panel on Climate Change (IPCC), Geneva, Switzerland, 2008. 3356

Neumann, F.: Lectures given in the 1860's CF Riemann-Weber, Die partiellen Differentialgleichungen Physik, C.F. Riemann-Weber, p. 121, 1860. 3354

Nicolsky, D., Romanovsky, V., and Panteleev, G.: Estimation of soil thermal properties using in-situ temperature measurements in the active layer and permafrost, Cold Reg. Sci. Technol., 55, 120–129, 2009. 3354, 3360

O'Donnell, J. A., Romanovsky, V. E., Harden, J. W., and McGuire, A. D.: The effect of moisture content on the thermal conductivity of moss and organic soil horizons from black spruce ecosystems in interior Alaska, Soil Sci., 174, 646–651, 2009. 3354, 3360

Overduin, P. P., Kane, D., and van Loon, W.: Measuring thermal conductivity in freezing and thawing soil using the soil temperature response to heating, Cold Reg. Sci. Technol., 45, 8–22, 2006. 3360

Painter, S. L.: Three-phase numerical model of water migration in partially frozen geological media: model formulation, validation, and applications, Comput. Geosci., 15, 69–85, 2011. 3358, 3360

Painter, S. L. and Karra, S.: Constitutive model for unfrozen water content in subfreezing unsaturated soils, Vadose Zone J., 13, doi:doi:10.2136/vzj2013.04.0071, 2014. 3358

Painter, S. L., Moulton, J., and Wilson, C.: Modeling challenges for predicting hydrologic response to degrading permafrost, Hydrogeol. J., 21, 1–4, 2013. 3358

Peters-Lidard, C., Blackburn, E., Liang, X., and Wood, E.: The effect of soil thermal conductivity parameterization on surface energy fluxes and temperatures, J. Atmos. Sci., 55, 1209–1224, 1998. 3354

Price, J. S., Whittington, P. N., Elrick, D. E., Strack, M., Brunet, N., and Faux, E.: A method to determine unsaturated hydraulic conductivity in living and undecomposed moss, Soil Sci. Soc. Am. J., 72, 487–491, 2008. 3354

Quinton, W., Gray, D., and Marsh, P.: Subsurface drainage from hummock-covered hillslopes in the Arctic tundra, J. Hydrol., 237, 113–125, 2000. 3360

Rawlins, M., Nicolsky, D., McDonald, K., and Romanovsky, V.: Simulating soil freeze/thaw dynamics with an improved pan-Arctic water balance model, Journal of Advances in Modeling Earth Systems (JAMES), 5, 659–675, 2013. 3354, 3373

Rinke, A., Kuhry, P., and Dethloff, K.: Importance of a soil organic layer for Arctic climate: a sensitivity study with an Arctic RCM, Geophys. Res. Lett., 35, L13709, doi:10.1029/2008GL034052 2008. 3354

Romanovsky, V. and Osterkamp, T.: Interannual variations of the thermal regime of the active layer and near-surface permafrost in northern Alaska, Permafrost Periglac., 6, 313–335, 1995. 3353

Romanovsky, V. and Osterkamp, T.: Thawing of the active layer on the coastal plain of the Alaskan Arctic, Permafrost Periglac., 8, 1–22, 1997. 3354

Romanovsky, V. E., Sazonova, T. S., Balobaev, V. T., Shender, N. I., and Sergueev, D. O.: Past and recent changes in air and permafrost temperatures in eastern Siberia, Global Planet. Change, 56, 399–413, doi:10.1016/j.gloplacha.2006.07.022, 2007. 3353

Schaefer, K., Zhang, T., Bruhwiler, L., and Barrett, A. P.: Amount and timing of permafrost carbon release in response to climate warming, Tellus B, 63, 165–180, 2011. 3353

Serreze, M., Walsh, J., Chapin Iii, F., Osterkamp, T., Dyurgerov, M., Romanovsky, V., Oechel, W., Morison, J., Zhang, T., and Barry, R.: Observational evidence of recent change in the northern high-latitude environment, Climatic Change, 46, 159–207, 2000. 3353

Shiklomanov, N. I., Anisimov, O. A., Zhang, T., Marchenko, S., Nelson, F. E., and Oelke, C.: Comparison of model-produced active layer fields: results for northern Alaska, J. Geophys. Res., 112, F02S10, doi:10.1029/2006JF000571, 2007. 3354

Slater, A. G. and Lawrence, D. M.: Diagnosing present and future permafrost from climate models, J. Climate, 26, 5608–5623, 2013. 3353

Stefan, J.: Über die Theorie der Eisbildung, insbesondere über die Eisbildung im Polarmeere, Ann. Phys.-Leipzig, 278, 269–286, 1891. 3354

Subin, Z., Koven, C., Riley, W., Torn, M., Lawrence, D., and Swenson, S.: Effects of soil moisture on the responses of soil temperatures to climate change in cold regions, in: AGU Fall Meeting Abstracts, vol. 1, American Geophysical Union, San Francisco, USA, p. 0418, 2012. 3354

The HadGEM2 Development Team: G. M. Martin, Bellouin, N., Collins, W. J., Culverwell, I. D., Halloran, P. R., Hardiman, S. C., Hinton, T. J., Jones, C. D., McDonald, R. E., McLaren, A. J., O'Connor, F. M., Roberts, M. J., Rodriguez, J. M., Woodward, S., Best, M. J., Brooks, M. E., Brown, A. R., Butchart, N., Dearden, C., Derbyshire, S. H., Dharssi, I., Doutriaux-Boucher, M., Edwards, J. M., Falloon, P. D., Gedney, N., Gray, L. J., Hewitt, H. T., Hobson, M., Huddleston, M. R., Hughes, J., Ineson, S., Ingram, W. J., James, P. M., Johns, T. C., Johnson, C. E., Jones, A., Jones, C. P., Joshi, M. M., Keen, A. B., Liddicoat, S., Lock, A. P., Maidens, A. V., Manners, J. C., Milton, S. F., Rae, J. G. L., Ridley, J. K., Sellar, A., Senior, C. A., Totterdell, I. J., Verhoef, A., Vidale, P. L., and Wiltshire, A.: The HadGEM2 family of Met Office Unified Model climate configurations, Geosci. Model Dev., 4, 723–757, doi:10.5194/gmd-4-723-2011, 2011. 3357

Tonkin, M. and Doherty, J.: Calibration-constrained Monte Carlo analysis of highly parameterized models using subspace techniques, Water Resour. Res., 45, W00B10, doi:10.1029/2007WR006678, 2009. 3359

Van Genuchten, M. T.: A closed-form equation for predicting the hydraulic conductivity of unsaturated soils, Soil Sci. Soc. Am. J., 44, 892–898, 1980. 3360

Verseghy, D. L.: CLASS a Canadian land surface scheme for GCMs. I. Soil model, Int. J. Climatol., 11, 111–133, 1991. 3357

Volodin, E., Dianskii, N., and Gusev, A.: Simulating present-day climate with the INMCM4.0 coupled model of the atmospheric and oceanic general circulations, Izv. Atmos. Ocean. Phys.+, 46, 414–431, 2010. 3357

Walker, W. E., Harremoes, P., Rotmans, J., Van Der Sluijs, J. P., Van Asselt, M. B. A., Janssen, P., and Mayer von Krauss, M. P.: Defining uncertainty: a conceptual basis for uncertainty management in model-based decision support, Inegrated Assessment, 4, 5–7, 2003. 3353

Watanabe, M., Suzuki, T., O'ishi, R., Komuro, Y., Watanabe, S., Emori, S., Takemura, T., Chikira, M., Ogura, T., Sekiguchi, M., Takata, K., Yamazaki, D., Yokohata, T., Nozawa,T.,

Hasumi, H., Tatebe, H., and Kimoto, M.: Improved climate simulation by MIROC5: mean states, variability, and climate sensitivity, J. Climate, 23, 6312–6335, 2010. 3357

Zhang, Y., Carey, S. K., Quinton, W. L., Janowicz, J. R., Pomeroy, J. W., and Flerchinger, G. N.: Comparison of algorithms and parameterisations for infiltration into organic-covered permafrost soils, Hydrol. Earth Syst. Sci., 14, 729–750, doi:10.5194/hess-14-729-2010, 2010. 3360

Table 1. NSMC parameter minimum and maximum bounds, units, and descriptions.

Parameter	Min	Max	Units	Description
ϕ_{peat}	0.7	0.93	–	Peat porosity
ϕ_{min}	0.19	0.76	–	Mineral porosity
$\Theta_{r,peat}$	0.04	0.4	$m^3\,m^{-3}$	Peat residual liquid saturation
$\Theta_{r,min}$	0.05	0.25	$m^3\,m^{-3}$	Mineral residual liquid saturation
K_{peat}	0.05	0.38	$W\,m^{-1}\,K^{-1}$	Peat thermal conductivity
K_{min}	0.2	4.0	$W\,m^{-1}\,K^{-1}$	Mineral thermal conductivity
$A_{peat,\,fr}$	0.1	3.0	–	Frozen peat thermal conductivity shape parameter
$A_{peat,\,un}$	0.1	1.5	–	Unfrozen peat thermal conductivity shape parameter
$A_{min,}$fr	0.1	3.0	–	Frozen mineral thermal conductivity shape parameter
$A_{min,}$un	0.1	1.5	–	Unfrozen mineral thermal conductivity shape parameter

Table 2. Linear regression intercept and slope coefficients for permafrost metrics as a function of calibration-constrained parameters. Slope coefficients are in bold since they describe the first-order dependence of metrics on parameters.

Metric	Parameter	Intercept	95 % Conf. Int.	**Slope**	95 % Conf. Int.	R^2
ALT	ϕ_{min}	1.66	1.65–1.67	**−1.39**	−1.41 to −1.37	0.95
$\overline{\mathcal{D}}$	ϕ_{min}	0.465	0.462–0.468	**−0.402**	−0.408 to −0.397	0.95
$\overline{S}_I$	$\Theta_{r,peat}$	0.510	0.506–0.513	**0.227**	0.215 to 0.240	0.52
	$\Theta_{r,min}$	0.452	0.450–0.455	**0.702**	0.687 – 0.717	0.87
S_T	ϕ_{min}	0.327	0.323–0.331	**−0.381**	−0.387 to −0.374	0.92

Discussion Paper | Discussion Paper | Discussion Paper | Discussion Paper |

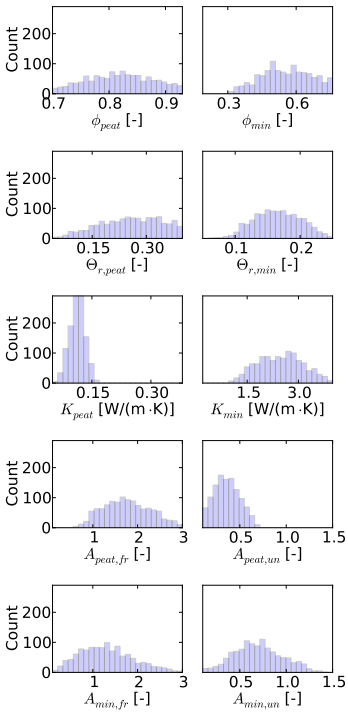

Figure 1. Histograms of calibration-constrained hydrothermal soil parameter combinations.

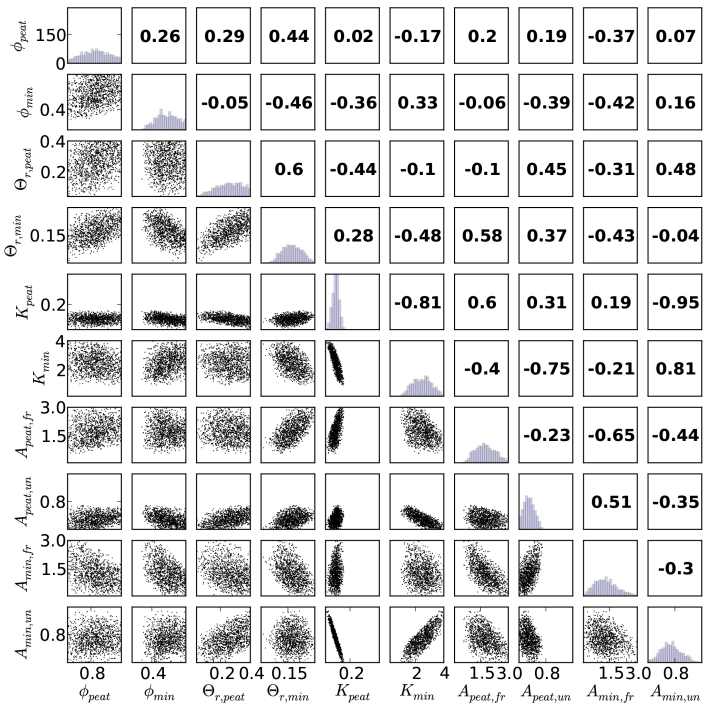

Figure 2. Matrix of paired plots of calibration-constrained hydrothermal soil parameter combinations. Parameter histograms are plotted along the diagonal, paired scatterplots in the lower triangle, and Pearson correlation coefficients in the upper triangle. The histogram counts for all histograms are indicated along the ordinate axis of the upper left plot.

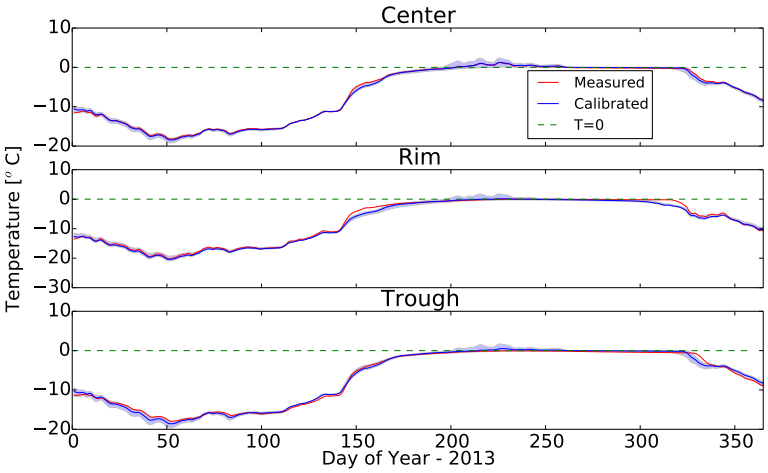

Figure 3. Time-series of temperature at 40 cm depths for the polygonal center, rim and trough profiles. Measured values are shown in red, calibrated in blue, and the 95 % confidence band is the shaded blue region.

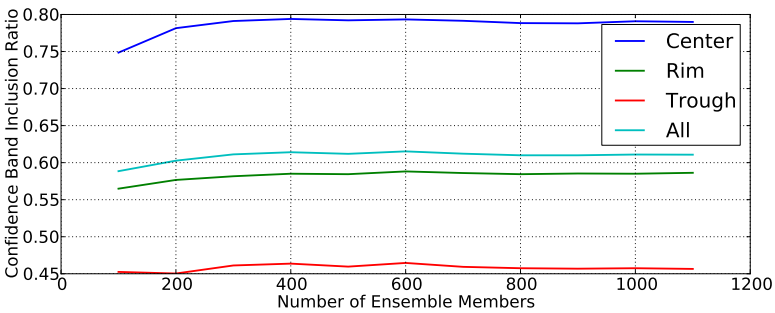

Figure 4. Calibration-constrained ensemble convergence analysis based on the ratio of measured temperatures within the 95 % confidence band for ensemble simulated temperatures.

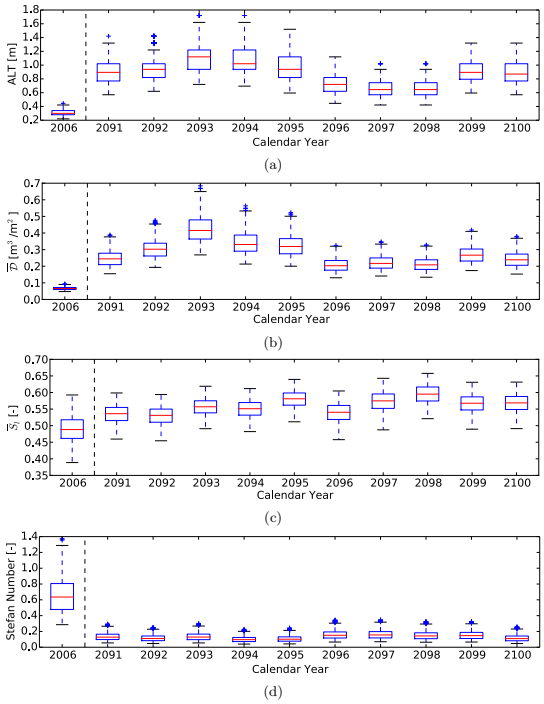

Figure 5. Boxplots of projected metrics including **(a)** ALT, **(b)** annual thaw depth-duration, **(c)** annual mean liquid saturation, and **(d)** Stefan number for year 2006 and from 2091 to 2100. The bottom and top of the boxes are the first and third quartiles, the red lines are medians, the whisker lengths are 1.5 times the interquartile range (50 %), and the plus symbols are outliers.

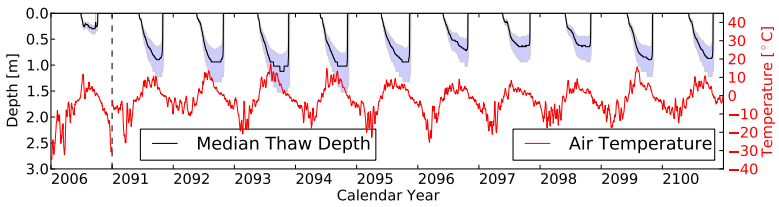

Figure 6. Thaw depth and air temperature time series for years 2006 and 2091 through 2100. The black line is the median thaw depth of the ensemble and the blue shaded region is the 95 % thaw depth confidence band for the ensemble.

Discussion Paper | Discussion Paper | Discussion Paper | Discussion Paper |

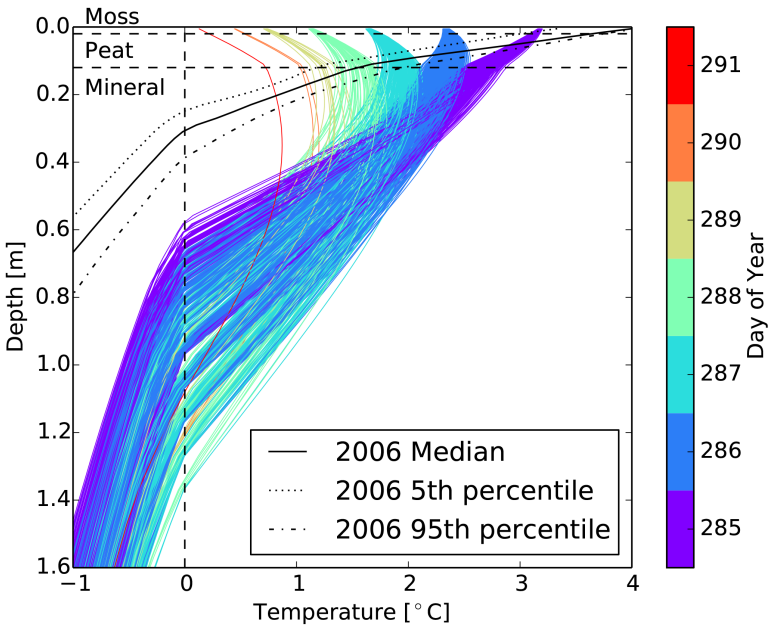

Figure 7. Intra-annual uncertainty due to soil properties for depth profiles of temperature for the ensemble when ALT occurs for calendar year 2100. The 2006 median and 5th and 95th percentiles are presented for reference. Day of year when ALT occurs for 2006 is from 246 to 260.

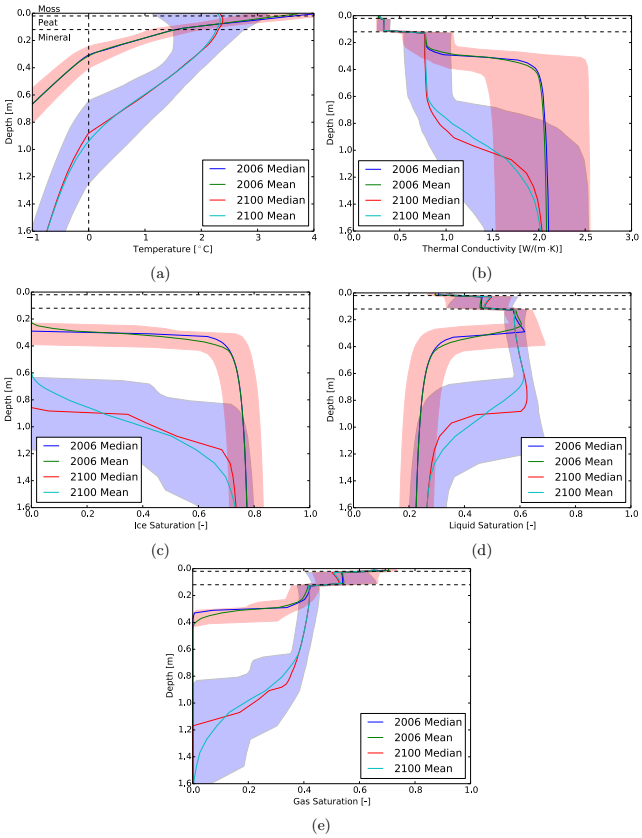

Figure 8. Intra-annual predictive uncertainty due to soil property uncertainty for depth profiles of ensemble statistical quantities when ALT occurs for calendar years 2006 and 2100. The shaded regions are the 95 % confidence intervals for 2006 (red) and 2100 (blue).

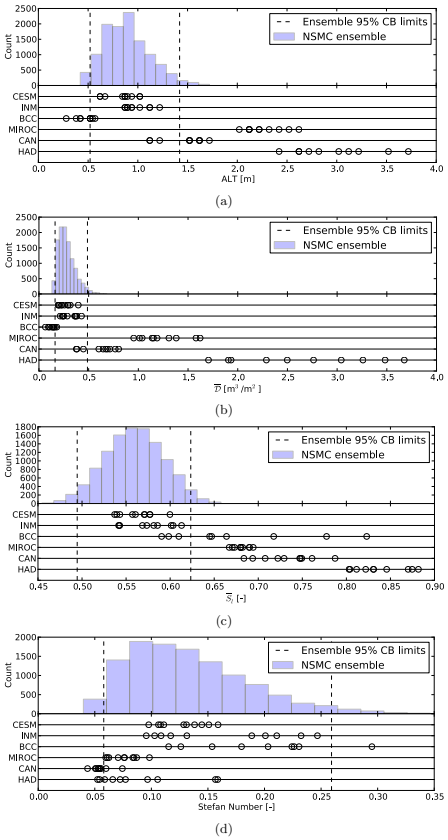

Discussion Paper | Discussion Paper | Discussion Paper | Discussion Paper |

Figure 9. Comparison of **(a)** ALT, **(b)** annual thaw depth-duration, **(c)** annual mean liquid saturation, and **(d)** Stefan number projection uncertainty due to soil property uncertainty (histograms) and structural climate model uncertainty (circles). Histograms include calibration-constrained ensemble values for years 2091 to 2100 (11 530 values) based on the CESM8.5 climate scenario. Open circles below the histograms are values for the various climate scenarios for the same years using the calibrated soil parameters (10 values each, except for BCC which has 9). Ensemble 95 % confidence band (CB) limits are indicated as vertical dashed lines.

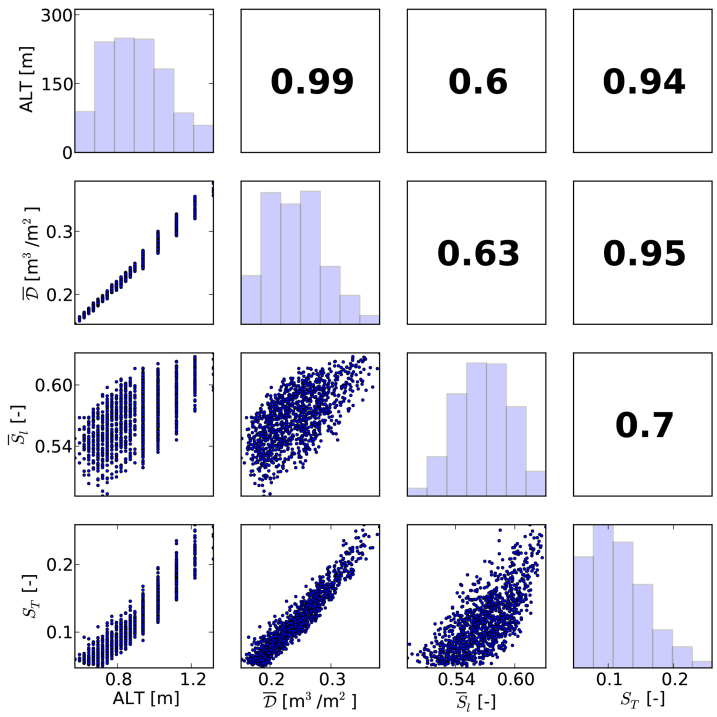

Figure 10. Matrix of paired plots of calibration-constrained ensemble projections for year 2100. Parameter histograms are plotted along the diagonal, paired scatterplots in the lower triangle, and Pearson correlation coefficients in the upper triangle. The range of counts for all histograms are as indicated along the ordinate axis of the upper left plot.

Discussion Paper | Discussion Paper | Discussion Paper | Discussion Paper |

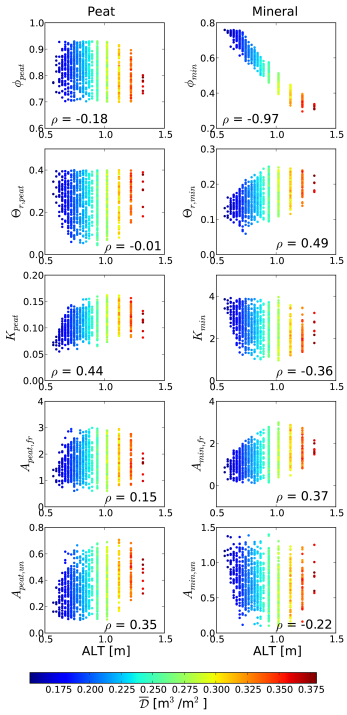

Figure 11. Scatterplots between calibration-constrained parameters and projected ALT for year 2100. Soil parameters associated with peat are on the left and with mineral soil on the right. Colors represent annual thaw depth-duration. The associated Pearson correlation coefficient ρ is indicated in each plot. The discrete nature of the ALT is due to the computational mesh discretization.

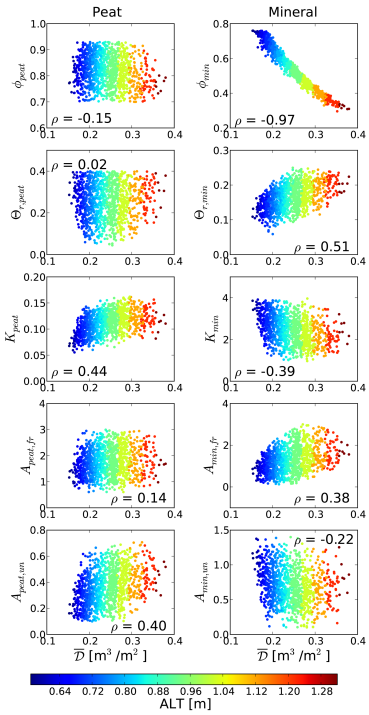

Figure 12. Scatterplots between calibration-constrained parameters and projected annual thaw depth-duration. Soil parameters associated with peat are on the left and with mineral soil on the right. Colors represent ALT. The associated Pearson correlation coefficient ρ is indicated in each plot.

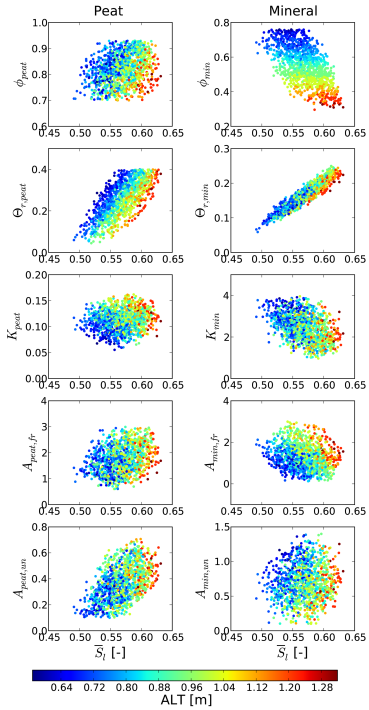

Figure 13. Scatterplots between calibration-constrained parameters and projected annual mean saturation. Soil parameters associated with peat are on the left and with mineral soil on the right. Colors represent ALT. The associated Pearson correlation coefficient ρ is indicated in each plot.

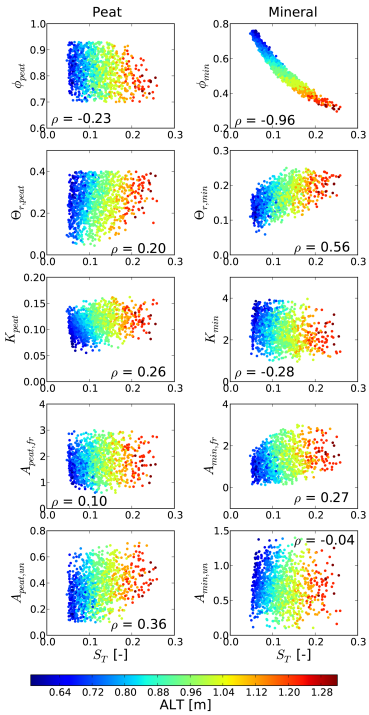

Figure 14. Scatterplots between calibration-constrained parameters and projected Stefan number. Soil parameters associated with peat are on the left and with mineral soil on the right. Colors represent ALT. The associated Pearson correlation coefficient ρ is indicated in each plot.

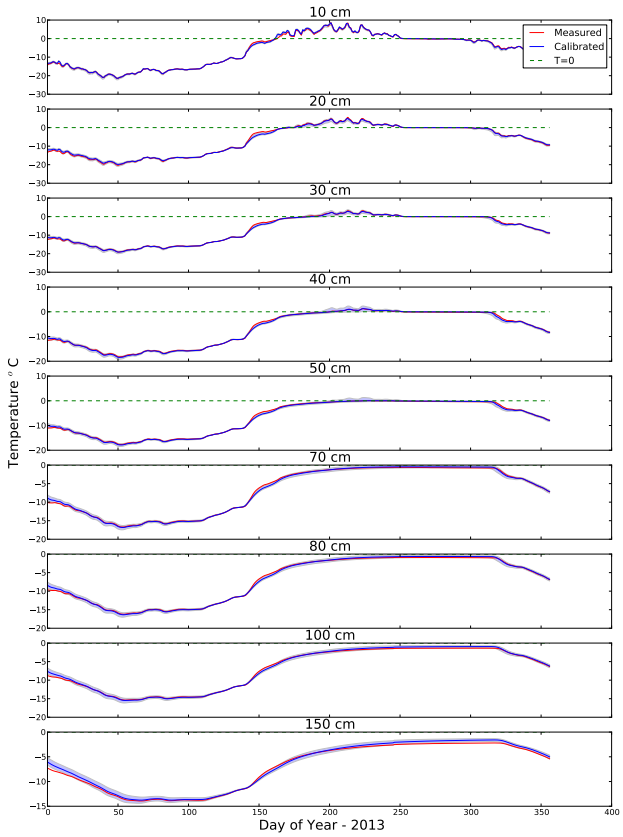

Figure A1. Time-series of temperature at specific depths for the polygonal center. Measured values from the field are shown as a red line, the mean of the NSMC sample as a blue line, and the 95 % confidence band is the shaded light blue region.

Discussion Paper | Discussion Paper | Discussion Paper | Discussion Paper |

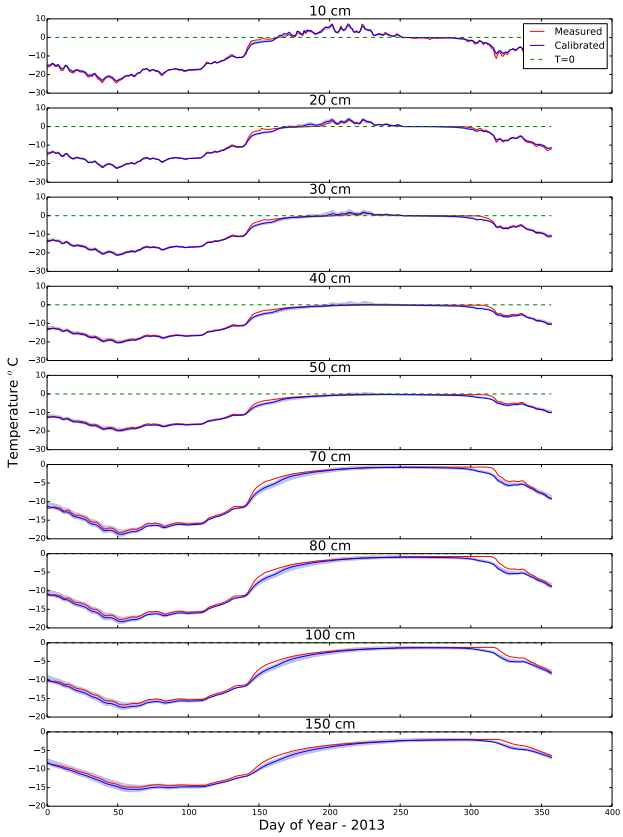

Figure A2. Time-series of temperature at specific depths for the polygonal rim. Measured values from the field are shown as a red line, the mean of the NSMC sample as a blue line, and the 95 % confidence band is the shaded light blue region.

Discussion Paper | Discussion Paper | Discussion Paper | Discussion Paper |

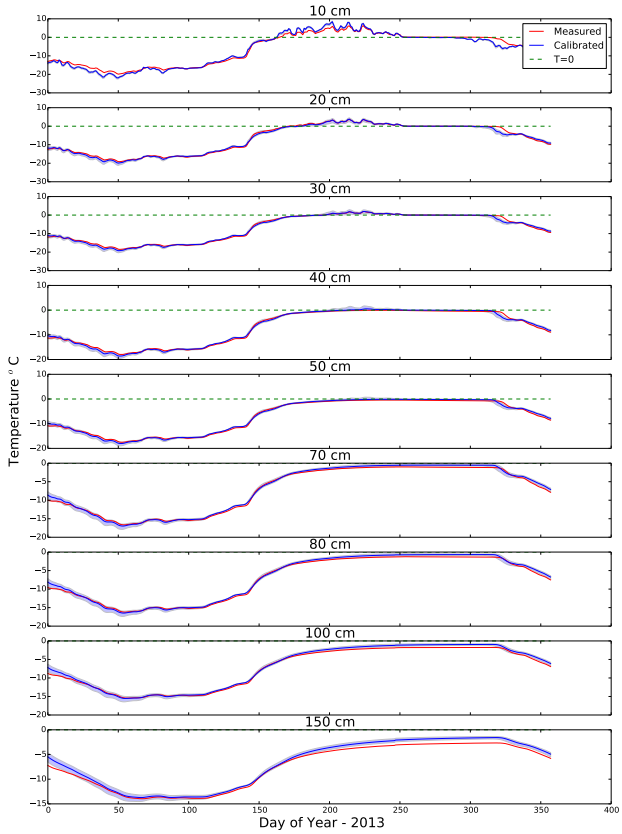

Figure A3. Time-series of temperature at specific depths for the polygonal trough. Measured values from the field are shown as a red line, the mean of the NSMC sample as a blue line, and the 95 % confidence band is the shaded light blue region.

Discussion Paper | Discussion Paper | Discussion Paper | Discussion Paper |